Performance and tolerance study of the rectilinear cooling channel for a muon collider

R. H. Zhu,[1, 2, *] H. Zhao,[1] C. Guo,[1, 2] J. D. Li,[1, 2] C. T. Rogers,[3, †] and J. C. Yang[1, ‡]

[1]*Institute of Modern Physics, Chinese Academy of Sciences, Lanzhou 730000, China*
[2]*University of Chinese Academy of Sciences, Beijing 100049, China*
[3]*STFC Rutherford Appleton Laboratory, Didcot OX11 0QX, United Kingdom*
(Dated: June 14, 2024)

The muon collider has the potential to be a powerful tool for the exploration of frontiers in particle physics. In order to reach the high luminosity, the 6D emittance of the muon beam needs to be reduced by several orders of magnitude. The cooling process for a muon collider involves two parts which are initial six-dimensional cooling and final transverse cooling. This paper focuses on the former and proposes a conceptual design of the rectilinear cooling channel with additional dipole magnets. In this paper, we first introduce a general method for designing the rectilinear cooling channel. Subsequently, we apply this method to develop two rectilinear cooling channels before and after the bunch merging system. Furthermore, we investigate the impact on cooling performance by employing π-mode RF cavities and considering the effect of errors in the magnetic and RF fields.

I. INTRODUCTION

Electron (e+e-) colliders offer several advantages over hadron colliders, primarily due to their ability to produce cleaner and simpler collision events. This makes it easier for physicists to analyze resulting particles. However, achieving multi-TeV collision energies is challenging for electron colliders due to the small mass of the electron, resulting in significant energy loss from synchrotron radiation [1]. Muons, on the other hand, have a much larger mass compared to electrons, making them less affected by synchrotron radiation. Additionally, muons have electron-like properties, making muon colliders a promising choice for high-energy physics research [2].

A technical challenge for the muon collider arises from the large emittance of the initial muon beam. This emittance significantly exceeds the acceptance limits of downstream accelerator components and is unsuitable for achieving high luminosity collisions, requiring a dedicated cooling channel to reduce the beam emittance. Additionally, due to the extremely short lifetime of muons (~2μs in the rest frame), the cooling process must be completed before the muons decay completely. This requirement makes ionization cooling the only feasible method to cool the muons. Ionization cooling can be classified into two types: 4D cooling and 6D cooling. In 4D ionization cooling, when the muon beam passes through an absorber, it simultaneously loses transverse and longitudinal momentum, with the longitudinal momentum restored by RF cavities. Consequently, the transverse phase space of the muons decreases over time. 4D ionization cooling was demonstrated by the Muon Ionization Cooling Experiment (MICE) collaboration [3, 4]. This arrangement does not achieve reduction of longitudinal emittance. In order to realize 6D ionization cooling, a dipole field and wedge-shaped absorber is envisaged to be introduced into the apparatus [5].

This setup ensures that particles with higher longitudinal momentum traverse a thicker part of the wedge, leading to greater longitudinal momentum loss. Consequently, both longitudinal and transverse emittance can be reduced simultaneously.

Four main types of ionization cooling channel have been developed in the past. The first one is ring-shaped cooing channel which uses tilted solenoids to generate the dispersion and bend the beam [6]. Simulations indicate that it successfully reduces the 6D emittance of the muons by a factor of ~50 [6]. However, significant challenge remains with injection into and extraction from the ring. To address this challenge, another cooling channel, known as the Guggenheim design [7], was proposed. Simulation results indicate that it achieves nearly the same cooling performance as the cooling ring [7]. However, as the cooling cells in Guggenheim are set on the vertical helix, it will be very difficult to construct. The third one is helical cooling channel. This is also a 6D cooling channel, but it uses helical magnets and homogeneous absorbers instead of solenoids and wedge absorbers [8]. The fourth one is rectilinear cooling channel. In this design, the components of the cooling cell are the same as those used in the cooling ring or Guggenheim. However, in the rectilinear design, the cooling cells are arranged along a straight line. The rectilinear channel, initially proposed by Balbekov [9], has a much simpler geometry compared to the Guggenheim design. This simplicity makes it easier to construct. Additionally, unlike the fixed focusing and dispersion in the cooling ring or Guggenheim, the rectilinear channel allows for adjustment of these parameters at different stages. This flexibility enables the rectilinear channel to reduce the emittance of muons to much smaller values [10, 11]. For this reason, we choose the rectilinear cooling channel as the baseline in our studies. Meanwhile, the International Muon Collider Collaboration (IMCC) proposes a muon 6D cooling demonstrator [12] using the π-mode RF [13], where the accelerating phase difference between two adjacent RF cells is π. The π-mode RF offers numerous advantages, such as its compact waveguide structure and the requirement for only one RF coupler and cryo-module feed-through to supply all the RF cells. However, it also has some disadvantages, including high RF power requirements for each coupler and a low transit time factor.

---

* zhuruihu@impcas.ac.cn
† Corresponding author.; chris.rogers@stfc.ac.uk
‡ Corresponding author.; yangjch@impcas.ac.cn

Since a low transit time factor might negatively impact beam dynamics, it is crucial to examine the impact on cooling performance with the π-mode RF. A tolerance study including magnetic and RF errors is also performed to assess the robustness of the cooling lattice using the π-mode RF. These studies also serve as preparation for future experiments on muon 6D cooling at the High Intensity heavy-ion Accelerator Facility (HIAF) [14].

This paper is structured as follows: Section II provides a review of the theory of 6D ionization cooling. Section III presents the parameters and simulation results of the proposed rectilinear cooling channel. In Section IV, we discuss the simulation results using the π-mode RF and analyze how magnetic and RF errors influence the cooling performance. Finally, Section V summarizes the conclusions drawn from this study.

II. PRINCIPLES OF 6D IONIZATION COOLING

The process of ionization cooling includes the gradual loss of both transverse and longitudinal momentum in muon beams, resulting from the ionization of atoms within the absorber material. While the longitudinal momentum can be compensated for in the RF cavities, the transverse momentum cannot. As a result, the muons' momentum becomes more parallel, leading to a reduction in emittance. The evolution of transverse emittance is described as follows [5]:

$$\frac{d\varepsilon_T}{ds} = -\frac{1}{\beta^2}\frac{dE_\mu}{ds}\frac{\varepsilon_n}{E_\mu} + \frac{1}{\beta^3}\frac{\beta_T E_s^2}{2E_\mu m_\mu c^2 L_R} \tag{1}$$

where ε_T is the normalized transverse emittance, E_μ is the muon beam energy, m_μ is the muon mass, β is the muon particle velocity, c is the speed of light, β_T is the transverse beta value, dE_μ/ds is the energy loss per unit length, L_R is the radiation length of absorber material and E_s is the characteristic scattering energy (~13.6 MeV).

The energy loss dE_μ/ds can be estimated by the Bethe-Bloch equation [15]:

$$\frac{dE_\mu}{ds} = 4\pi N_A r_e^2 m_e c^2 \rho \frac{Z}{A}\left[\frac{1}{\beta^2}\ln\left(K\gamma^2\beta^2\right) - 1 - \frac{\delta}{2\beta^2}\right] \tag{2}$$

where r_e is the classical electron radius, ρ is the density, N_A is Avogadro's number, A is the atomic weight, Z is the atomic number and m_e is the electron mass. $K = 2m_e c^2/I$ and I is the mean excitation energy. δ is the density effect factor which can be omitted for the muons with longitudinal momentum being around 200 MeV.

The first segment of Eq. (1) can be interpreted as the cooling term, while the second segment represents the heating term. The equilibrium transverse emittance is defined when dE_μ/ds in Eq.(1) is 0 [5]:

$$\varepsilon_{T,eq} = \frac{\beta_T E_s^2}{2\beta m_\mu c^2 L_R \left|\frac{dE_\mu}{ds}\right|} \tag{3}$$

From Eq. (3), it is evident that in order to achieve a lower equilibrium transverse emittance, two key factors should be

considered. Firstly, the focusing at the absorber should be strong, indicated by a smaller transverse beta value. Secondly, the absorber material should possess a large product of L_R and $\left|\frac{dE_\mu}{ds}\right|$, which is satisfied by materials with low atomic numbers, such as liquid hydrogen and lithium hydride.

For a muon collider, it is crucial to also decrease the longitudinal emittance to meet the required acceptance of downstream accelerator components. To achieve longitudinal cooling, a well-known scheme called emittance exchange is employed. This involves using wedge-shaped absorbers and introducing dispersion. The introduction of dispersion causes the beam to spread transversely, allowing particles with higher momentum to pass through a thicker part of the absorber and lose more energy, thereby reducing the longitudinal emittance at the cost of increasing the transverse emittance. The value of dispersion must be carefully chosen to simultaneously achieve both transverse and longitudinal cooling, also known as 6D cooling.

For the 6D cooling using the wedge, formulas for the evolution of transverse and longitudinal emittance have been provided in [5, 11, 16] and are shown as below:

$$\frac{d\varepsilon_T}{ds} = -\frac{g_T}{\beta^2 E_\mu}\frac{dE_\mu}{ds}\varepsilon_T + \frac{\beta_T E_s^2}{2\beta^3 m_\mu c^2 L_R E_\mu} \tag{4}$$

where transverse partition number $g_T = 1 - D/w$, D is the dispersion and w is the distance between the beam center and the apex of the wedge.

$$\frac{d\varepsilon_L}{ds} = -\frac{g_L}{\beta^2 E_\mu}\frac{dE_\mu}{ds}\varepsilon_L + \frac{\beta_L}{2}\frac{d\left\langle\Delta E^2\right\rangle}{ds} \tag{5}$$

where ε_L is the longitudinal emittance, g_L is the longitudinal partition number and β_L is the longitudinal beta function. Longitudinal partition number and beta function can be expressed as [16]:

$$g_L = \frac{2\gamma^2 - 2\ln[K(\gamma^2-1)]}{\gamma^2\ln[K(\gamma^2-1)] - (\gamma^2-1)} + \frac{D}{w} \tag{6}$$

$$\beta_L = \sqrt{\frac{\lambda_{RF}\beta^3\gamma m_\mu c^2 \alpha_p}{2\pi e V' \cos\varphi_s}} \tag{7}$$

where α_p is the slip factor, which can be estimated as $-1/\gamma^2$ (γ being the Lorentz factor) since it is an approximation in the linac and the rectilinear cooling channel is roughly a linac, V' is the average RF gradient, φ_s is the RF phase and λ_{RF} is the RF wavelength.

The second term in Eq. (5) arises from random fluctuations in the energy loss known as energy straggling. It can be approximately described as [17]:

$$\frac{d\left\langle\Delta E^2\right\rangle}{ds} = 4\pi (r_e \gamma m_e c^2)^2 n_e \left(1 - \frac{\beta^2}{2}\right) \tag{8}$$

The equillibrium emittance can be derived when $d\varepsilon/ds = 0$, so, from Eq. (4) and Eq. (5), we get [16]:

$$\varepsilon_T^{eq} = \frac{\beta_T E_s^2}{2\left|\frac{dE_\mu}{ds}\right|\beta g_T m_\mu c^2 L_R} \quad (9)$$

$$\varepsilon_L^{eq} = \frac{\beta_L m_e c^2 \gamma^2 (1 - \frac{\beta^2}{2})}{2g_L \beta m_\mu c^2 [\frac{\ln(K\gamma^2\beta^2)}{\beta^2} - 1]} \quad (10)$$

The expressions for the evolution of transverse and longitudinal emittance can also be obtained from Eq. (4) and Eq. (5) [16]:

$$\varepsilon_i(s) = (\varepsilon_{i,0} - \varepsilon_{i,eq})\exp\left(-\frac{s}{L_{cool,i}}\right) + \varepsilon_{i,eq} \quad (11)$$

where $i = T$ or L corresponding to the transverse or longitudinal direction, $\varepsilon_{i,0}$ is the initial emittance and $L_{cool,i}$ is the cooling length shown in Eq. (12).

$$L_{cool,i} = \left(\frac{g_i}{\beta^2 E_\mu}\left\langle\frac{dE_\mu}{ds}\right\rangle\right)^{-1} \quad (12)$$

where dE_μ/ds with angular brackets is the energy loss averaging over the full transport length.

III. LINEAR LATTICE OPTICS AND GENERAL DESIGN METHODS

A. Lattice function and beam dynamics

Studying the fundamental lattice features and beam dynamics in the rectilinear cooling channel is essential as it provides valuable guidance for the design and simulation of the channel, aiding in optimizing its performance and efficiency. We analyze the lattice function and beam dynamics of the channel without wedges and RF.

1. Transverse beta function, phase advance and momentum acceptance

The beta function is a crucial parameter in accelerator physics as it represents the focusing strength of the external magnetic field. In the case of solenoids, where the focusing strength is equal in both the x and y directions, it is more common to use the transverse beta function β_T instead of individual beta function β_x and β_y. The transverse beta function evolves as [18]:

$$2\beta_T\beta_T'' - \beta_T'^2 + 4\beta_T^2 k^2 - 4(1 + L^2) = 0 \quad (13)$$

where L is the normalized canonical angular momentum and k is the solenoid focusing strength,

$$k = \frac{qcB_z}{2p_z} \quad (14)$$

where q is the charge of the particle, c is the speed of light, B_z is the longitudinal magnetic field and p_z is the longitudinal momentum.

Assuming $L = 0$, one can solve Eq. (13) periodically to obtain the value of transverse beta function along the cooling cell.

Phase advance φ is defined as:

$$\varphi = \int \frac{1}{\beta_T}dz \quad (15)$$

When the phase advance is close to or equal to $n\pi$ ($n = 1, 2, 3, ...$), the value of transverse beta function increases significantly leading to the integer or half-integer resonance. The width of resonance stopband Δ can be approximately described as [19]:

$$\Delta \cong n\frac{\theta_n}{\theta_0} \quad (16)$$

where n is the order of the approximation (usually $n = 2, 3$) and θ_n is the Fourier coefficient of solenoid focusing strength k along the channel,

$$\left(\frac{L}{\pi}\right)^2 k(z)^2 = \sum_{n=-\infty}^{+\infty} \theta_n e^{\frac{i2n\pi z}{L}} \quad (17)$$

where L is the length of the cooling cell.

It is evident that the phase advance of the cooling cell is dependent on the beam longitudinal momentum, as indicated by Eq. (13), Eq. (14) and Eq. (15). The momentum acceptance is defined as the range of beam longitudinal momentum values where the phase advance deviates from the resonance condition. It is crucial to ensure that the momentum acceptance remains sufficiently large (e.g., 5 or 6 times larger than the RMS longitudinal momentum spread) in order to minimize particle loss.

2. Closed orbit and dispersion

Given the symmetry of the magnetic field in the y direction around the middle point of the cooling cell (shown in Fig. (2)), it is necessary for the closed orbits in both the x and y directions to exhibit symmetry as well. This symmetry requires the derivatives of closed orbits at the boundary of the cooling cell must be zero. Consequently, this simplifies the search for closed orbits, as the initial momenta in both the x and y directions can be set to zero. If the beam center is placed on the closed orbit, most particles in the beam will perform betatron oscillation around the closed orbit, resulting in the overall beam motion being nearly periodic and leading to reduced particle loss. The horizontal and vertical dispersion components can be calculated from the closed orbit as:

$$D_x = \frac{\Delta x}{\Delta p/p} \tag{18}$$

$$D_y = \frac{\Delta y}{\Delta p/p} \tag{19}$$

where Δx, Δy and Δp represent the difference of the closed orbit in x and y direction, respectively, and momentum relative to the reference particle.

B. Cooling channel design process

The design process consists of four steps as follows:

a) Calculation of transverse beta function and momentum acceptance: The first step is to choose an appropriate transverse beta function value at the center of the wedge and a sufficient momentum acceptance. We use the well-known differential evolution algorithm [20] to adjust the relative solenoid parameters (position, current density and length) and the target functions which need to be minimized are:

$$f = (\beta_T - \beta_{T,ref})^2 + (\varphi_{left} - \pi)^2 \tag{20}$$

$$f = (\beta_T - \beta_{T,ref})^2 + (\varphi_{left} - 2\pi)^2 + (\varphi_{right} - \pi)^2 \tag{21}$$

where $\beta_{T,ref}$ is the transverse beta function value we choose, φ_{left} and φ_{right} denote the phase advances of the cooling cell, which are obtained from the left-most and right-most momenta of the chosen momentum acceptance. Eq.(20) is for the phase advance of the cooling cell below π and Eq.(21) is for the phase advance between π and 2π. As we are only considering linear resonance, the resonance stop band described by Eq. (16) is not included in the target function.

b) Calculation of closed orbit and dispersion: The second step is to settle the value for the dispersion which decides the emittance exchange rate. As the dispersion is calculated from closed orbit difference shown in Eqs. (18) and (19), we need to find the closed orbit first. The target function used to find the closed orbit is:

$$f = (x_{final} - x_{init})^2 + (y_{final} - y_{init})^2 + (P_{z,final} - P_{z,init})^2 \tag{22}$$

The dispersion is controlled by the strength of the dipole field. It should be noted that the cell lattice used in this step is without the wedges and RF cavities.

c) Obtaining the list of RF parameters: The dispersion in the RF cavities region results in a coupled transverse and longitudinal beam motion. This means that finding the proper RF parameters involves more than just compensating for energy loss in the wedge absorber. It also requires maintaining the same closed orbit as in step b). We manually set the dispersion and choose the maximum accelerating gradient and accelerating phase as two variables. The wedge absorber length is adjusted manually in a certain range. The target function for

finding the closed orbit in this step is the same as Eq. (22). Additionally, since selecting the correct z-momentum of the reference particle affects the timing of the RF cavities, we iterate over a certain range of the reference particle's z-momentum to obtain several lists of RF parameters. In this step, for each wedge absorber length, several lists of RF parameters corresponding to different reference momenta are obtained.

d) Running the multi-particle tracking simulation: The lists obtained from step c) are utilized as inputs for the RF cavities, and the multi-particle tracking simulation is initiated. G4Beamline-3.08 [21] is employed to complete the tracking simulation, while the emittance calculation is carried out using the code Ecalc9f [22]. We introduce a merit factor to select the best outcome and quantify cooling efficiency. It is described as [2]:

$$M(s) = \frac{T(s)^2}{\frac{\varepsilon_T(s)}{\varepsilon_T(0)}\sqrt{\frac{\varepsilon_L(s)}{\varepsilon_L(0)}}} \tag{23}$$

where T is the transmission, $\varepsilon_T(s)$ and $\varepsilon_T(0)$ are the normalized transverse emittance at a specific position and start of the cooling section, respectively, while $\varepsilon_L(s)$ and $\varepsilon_L(0)$ refer to the normalized longitudinal emittance. This merit factor is indicative of the improvement in luminosity arising from the cooling provided by the rectilinear cooling channel.

All calculations and simulations in the above steps are performed in parallel using two AMD EPYC 7642 processors with a total of 96 cores.

IV. LATTICE PARAMETERS AND TRACKING STUDIES OF THE RECTILINEAR COOLING CHANNEL

A. Layout of the cooling cell

The basic lattice layout of one cell used in this paper is depicted in Fig. (1) which resembles the previous design [11]. However, instead of tilting solenoids to generate dipole field, additional dipole magnets are incorporated for easier tuning the dipole field.

As shown in Fig. (1), each cooling cell consists of solenoids with opposite polarity, dipole magnets for dispersion generation, RF cavities for beam energy loss compensation and liquid hydrogen (LH$_2$) wedge absorbers. This paper utilizes two types of cooling cell layouts. The primary distinction between these layouts lies in the positioning of the wedge absorbers. When the transverse beta function has three minima, we employ the layout depicted in Fig. (1a). When the transverse beta function has two minima, we choose the layout shown in Fig. (1b). We prefer the configuration where the transverse beta has three minima, because it enables us to put a wedge aborber at the middle of the cell. This arrangement results in the reduction of the length of each wedge absorber, consequently lowering the average transverse beta function as described by Eq. (24).

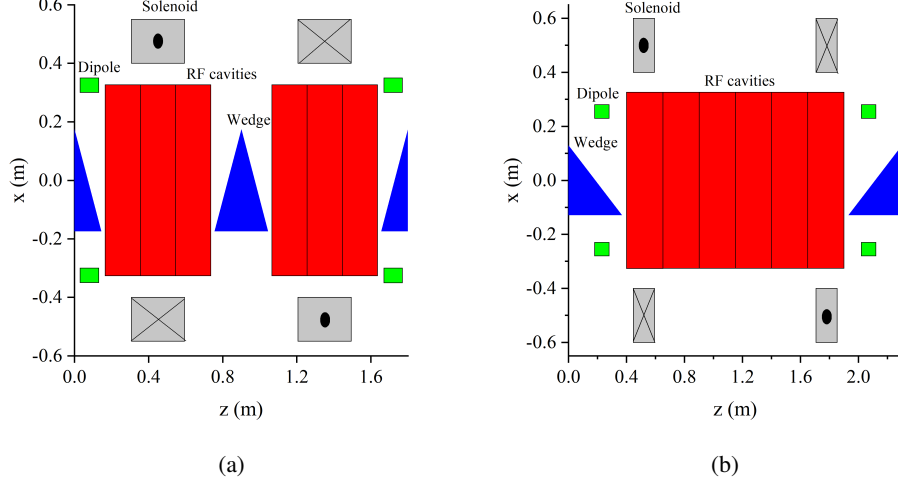$$\beta_{T,ave} = \frac{\int_0^L \beta_T \, dz}{L} \tag{24}$$

FIG. 1: Schematics of two types of the cooling cell layout: (a) suitable for the case where the transverse beta function has 3 minima; (b) suitable for the case where the transverse beta function has 2 minima

where L is the length of the absorber.

Windows are also taken into account for both the liquid hydrogen absorbers and RF cavities, although they are not displayed in Fig. (1). Beryllium (Be) is chosen as the window material for the absorber due to its low atomic number, which has minimal impact on the cooling performance. It is also selected as the window material for the RF because it can increase the operational gradient [23]. For the absorber, the window thickness varies from 300 μm (stage 1 in pre-merging section) to 40 μm (stage 10 in post-merging section). For the RF, the window thickness varies from 120 μm (stage 1 in pre-merging section) to 10 μm (stage 10 in post-merging section). The geometry of the absorber and RF windows are both simple disks. Each absorber and RF cavity is enclosed with two windows at both ends. The windows of the wedge absorbers are oriented to completely cover the sides of the triangular prism-shaped wedges.

In characterizing the fringe field of the dipole magnets, we employ the expressions derived from [24]. The fringe field components are described by the following equations:

$$B_y = B_0 \frac{1 + e^{a_1 z} \cos a_1 y}{1 + 2e^{a_1 z} \cos a_1 y + e^{2a_1 z}} \tag{25}$$

$$B_z = B_0 \frac{-e^{a_1 z} \sin a_1 y}{1 + 2e^{a_1 z} \cos a_1 y + e^{2a_1 z}} \tag{26}$$

where B_0 is the nominal dipole field strength, a_1 is a coefficient in Enge function [25] and the z and y are the coordinates normalized by the dipole magnet aperture. It should also be noted that, for simplicity, we set all other coefficients to 0 except for a_1, which is equal to 5. It is also noteworthy that while only the integrated dipole field significantly influences the closed orbit of the particles motion, utilizing fully Maxwellian fringe field expressions is always more physical.

B. Design of the pre-merging cooling section

We use the output beam file from the front end of the previously proposed Neutrino factory [26] as the starting point for our tracking simulation, following a similar approach to the previous design [11]. However, we have made changes by selecting 352 MHz and 704 MHz as our RF frequencies instead of the 325 MHz and 650 MHz used in the previous design. To match the new 352 MHz RF, we adjust the input beam by compressing it in time by a factor of 325/352 and stretching its z-momentum by 352/325. This ensures the input beam matches the new 352 MHz RF frequency while keeping its longitudinal phase space volume conserved.

A 4-stage rectilinear channel is utilized to cool the beam to meet the required initial emittance for the bunch merging system. Given the large emittance of the input beam, it is necessary to avoid over-focusing in the first stage. Therefore, a relatively large beta function value of 70 cm is chosen at the wedge. The layout of the cooling cell in stage 1 is depicted in Fig. (1a), including two solenoids with opposite polarity, two positive dipole magnets, six 352 MHz RF cavities, and two liquid hydrogen wedge absorbers. Detailed parameter information is provided in Table I. Fig. (2a) illustrates the on-axis B_z generated from the solenoid coils in G4Beamline and the B_y generated from Eqs. (25) and (26) of the cooling cell in stage 1 in the pre-merging section. The shape of the on-axis B_z is sinusoidal and flips at the middle of the cell to eliminate angular momentum accumulation. The maximum on-axis B_z is 2.5 T, corresponding to a large beta function value. As shown in Fig. (3a), the beta function has three minima where the wedge absorbers are placed. Fig. (3b) shows the dependence of beta and the phase advance on momentum. The transverse beta function at the wedge absorber is approximately proportional to the z-momentum. The phase advance at 145 MeV/c exceeds π, indicating a momentum ac-

TABLE I: Main parameters for the cooling cells in each stage. A and B denote the pre-merging and post-merging section respectively. Liquid hydrogen is used as the wedge absorber material for all stages.

|	Cell length (m)	Stage length (m)	Pipe radius (cm)	Max. on-axis B_z (T)	Integrated B_y (T·m)	Transverse beta (cm)	Dispersion (mm)	On-axis wedge length (cm)	Wedge apex angle (deg)	RF frequency (MHz)	Number of RFs	RF length (cm)	Max. RF gradient (MV/m)	RF phase (deg)
A-Stage 1	1.8	104.4	28	2.5	0.102	70	-60	14.5	45	352	6	19	27.4	18.5
A-Stage 2	1.2	106.8	16	3.7	0.147	45	-57	10.5	60	352	4	19	26.4	23.2
A-Stage 3	0.8	64.8	10	5.7	0.154	30	-40	15	100	704	5	9.5	31.5	23.7
A-Stage 4	0.7	86.8	8	7.2	0.186	23	-30	6.5	70	704	4	9.5	31.7	25.7
B-Stage 1	2.3	55.2	23	3.1	0.106	35	-51.8	37	110	352	6	25	21.6	28.2
B-Stage 2	1.8	61.2	19	3.9	0.138	30	-52.4	32	120	352	5	22	23.3	30.9
B-Stage 3	1.4	75.6	12.5	5.1	0.144	20	-40.6	24	115	352	4	19	24.9	29.8
B-Stage 4	1.1	67.1	9.5	6.6	0.163	15	-35.1	20	110	352	3	22	24.3	31.3
B-Stage 5	0.8	44	6	9.1	0.116	10	-17.7	12	120	704	5	9.5	22.5	24.3
B-Stage 6	0.7	38.5	4.5	11.5	0.0868	6	-10.6	11	130	704	4	9.5	31.2	19.8
B-Stage 7	0.7	35.7	3.7	13	0.0882	5	-9.8	10	130	704	4	9.5	29.5	17.8
B-Stage 8	0.65	44.85	2.65	15.8	0.0726	3.8	-7.0	7	140	704	4	9.5	28.1	14.0
B-Stage 9	0.65	34.45	2.25	16.6	0.0694	3	-6.1	7.5	140	704	4	9.5	29.7	11.9
B-Stage 10	0.63	30.87	2.1	17.2	0.0691	2.7	-5.7	6.8	140	704	4	9.5	24.9	12.2

(a)   (b)
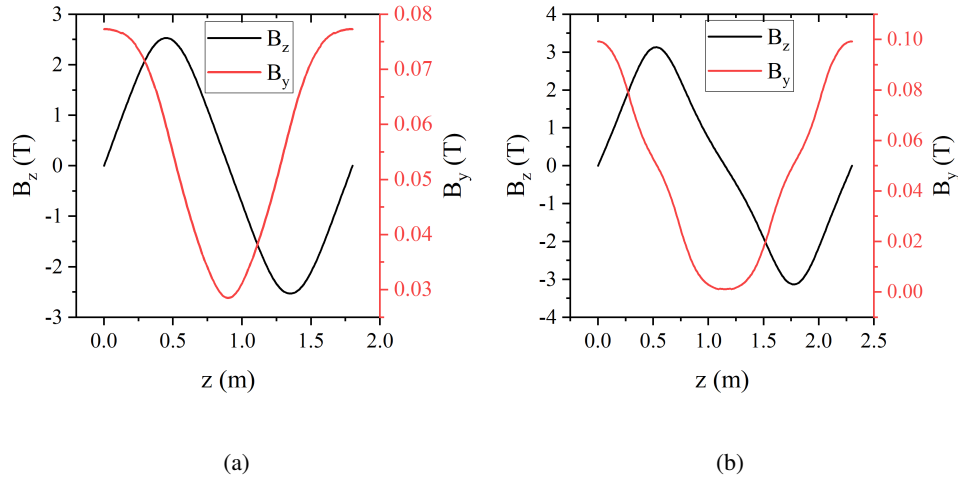
FIG. 2: On-axis B_z and B_y of the cooling cell (black solid line: on-axis B_z, red solid line: B_y): (a) stage 1 in pre-merging section; (b) stage 1 in post-merging section

TABLE II: Simulation results on the normalized emittance and transmission at the end of each stage berfore merging

	$\varepsilon_{T,sim}$ (mm)	$\varepsilon_{L,sim}$ (mm)	$\varepsilon_{6D,sim}$ (mm^3)	Transmission
Start	16.96	45.53	13500	
A-Stage 1	5.165	18.31	492.6	75.2%
A-Stage 2	2.473	7.113	44.03	84.4%
A-Stage 3	1.556	3.880	9.594	85.6%
A-Stage 4	1.239	1.741	2.861	91.3%

ceptance above 145 MeV/c. Fig. (3c) shows how the closed orbit changes in the x and y directions for momenta of 200 MeV/c, 210 MeV/c, and 190 MeV/c. As expected, only the x-direction orbit varies noticeably since the dipole field acts only in the y-direction. From Fig. (3d), we see the dispersion in the x-direction also has three minima, while dispersion in the y-direction remains close to zero. Stage 1 terminates at 104.4 m and connects with a later stage which has a smaller beta function value at the wedge absorber. Stage 4 has the highest B_z field (7.2 T for the on-axis field) and smallest transverse beta function (23 cm at the wedge absorber) before the bunch merging in order to decrease the transverse and longitudinal emittance of the muon beam to the required values for the bunch merging system (normalized transverse emittance ~=1.3 mm and normalized longtudinal emittance ~=1.7 mm) [27]. It is worth mentioning that we double the RF frequency from 352 MHz to 704 MHz for stages 3 and 4. This allows
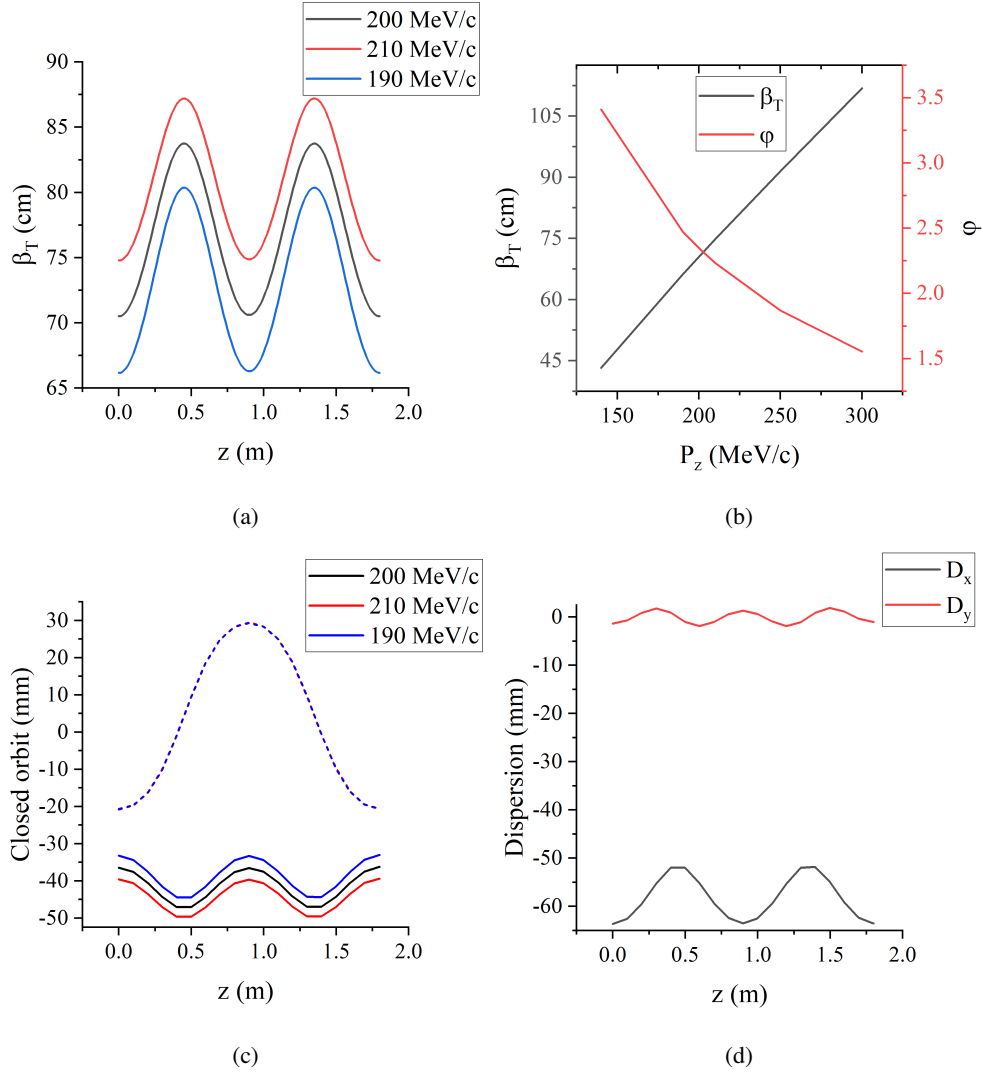
FIG. 3: Evolution of lattice parameters of the cooling cell in stage 1 before bunch merging: (a) transverse beta function versus position for 3 different z-momenta; (b) transverse beta function at the wedge absorber and phase advance of the cooling cell versus z-momentum; (c) closed orbit versus position for 3 different z-momenta (solid line: x plane, dashed line: y plane); (d) dispersion versus position (calculated at z-momentum of 200 MeV/c)

for an increase in the RF accelerating gradient and a decrease in the longitudinal beta function, as indicated by Eq. (7). This adjustment contributes to reducing the longitudinal emittance.

The final emittance and transmission of each stage are listed in Table II. The evolution of the transverse and longitudinal emittance is shown in Fig. (5a). As depicted in Fig. (5a), a significant spike is evident at the junction of stage 3 and stage 4. This spike is due to the longitudinal mismatching as we start to use the 704 MHz RF in the stage 4. In summary, the pre-merging cooling section consists of 4 stages with a total length of 362.8 m. It effectively reduces the transverse and longitudinal emittance from 16.96 mm and 45.53 mm to 1.239 mm and 1.741 mm, respectively, with an overall transmission rate of 49.6% including the muon decays. The particle distribution in phase spaces at the beginning and end of the cooling section is illustrated in Fig. (7a), (7b) and (7c). It is encour-

aging to observe from Fig. (6a) that the merit factor increases at the end of each stage indicating each cooling stage is well-designed. Similar to the emittance evolution Fig. (5a), the merit factor in Fig. (6a) drops significantly at the start of the stage 3 mostly because of the longitudinal mismatching resulting from the sudden jump in RF frequency from 352 MHz to 704 MHz.

C. Design of the post-merging cooling section

After the bunch merging system, both the transverse and longitudinal emittance of the muon beam increase by a factor of ~4 [27]. We choose to maintain the phase advance of the cooling cell in the post-merging section between π and 2π to achieve a smaller transverse beta function. Despite the
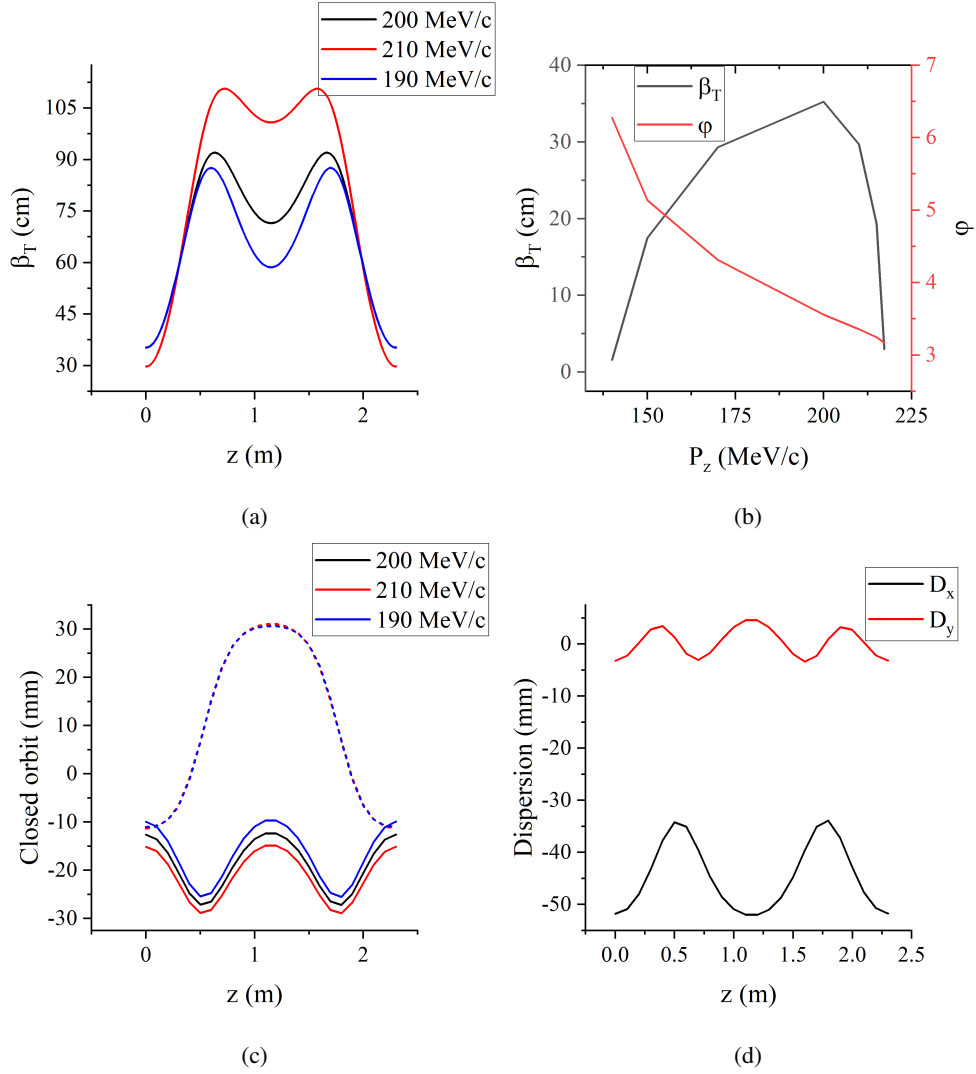
FIG. 4: Evolution of lattice parameters of the cooling cell in stage 1 after bunch merging: (a) transverse beta function versus position for 3 different z-momenta; (b) transverse beta function at the wedge absorber and phase advance of the cooling cell versus z-momentum; (c) closed orbit versus position for 3 different z-momenta (solid line: x plane, dashed line: y plane); (d) dispersion versus position (calculated at z-momentum of 200 MeV/c)

fact that this choice results in a narrower longitudinal momentum acceptance, the significantly smaller initial longitudinal emittance in the post-merging section, compared to the pre-merging section, allows for such an approach. We also find it is difficult to have 3 minima for the transverse beta function but 2 minima at the beginning and the end of the cell. This difficulty arises from the periodicity of B_z. So, we choose the cell layout shown in Fig. (1b) for all stages in this section. Moreover, since the output beam of the post-merging rectilinear cooling section serves as the input beam for the final cooling section through deceleration, our objective is to minimize the emittance of the output beam of the post-merging rectilinear cooling section while mitigating beam loss. In other words, our aim is to ensure that the merit factor defined in Eq.(23) increases along the channel.

A 10-stage rectilinear cooling channel is used in the post-

merging section and its main parameters are summarized in Table I. Given that the initial transverse emittance of this section is approximately one third of that in the pre-merging stage, a smaller transverse beta function value of 35 cm is chosen for stage 1. The on-axis field profile of stage 1 is illustrated in Fig. (2b). In comparison with the pre-merging stage 1, the field shape remains similar but has a higher on-axis B_z, a consequence of the smaller transverse beta function. Figure (4a) depicts the evolution of the transverse beta function along the cooling cell in stage 1. It is evident that the transverse beta function of the 210 MeV/c beam is significantly larger than that of the 200 MeV/c beam due to its proximity to the π resonance. Furthermore, Fig. (4b) illustrates transverse beta function and phase advance versus momentum in stage 1. The phase advance of the 140 MeV/c and 220 MeV/c beams approaches 2π and π, respectively, indicating a momentum
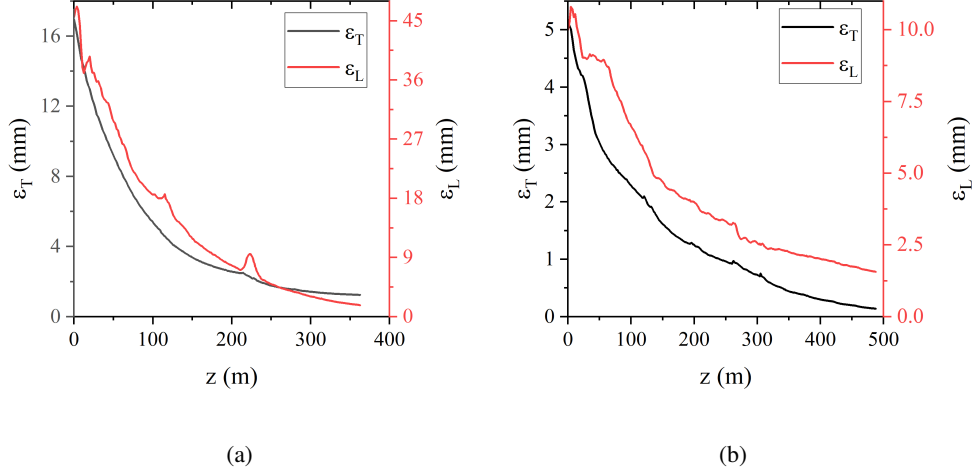
FIG. 5: Evolution of the normalized transverse and longitudinal emittance: (a) emittance evolution in pre-merging section; (b) emittance evolution in post-merging section
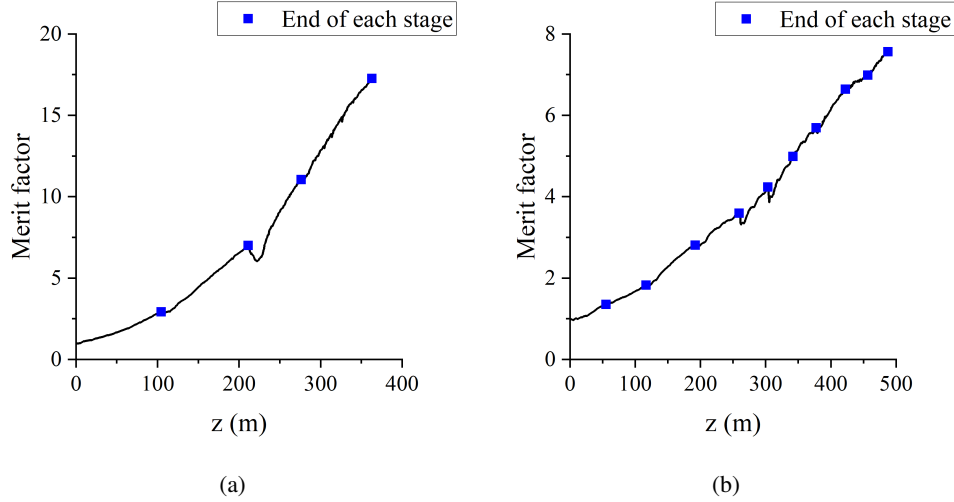

FIG. 6: Evolution of the merit factor: (a) pre-merging section; (b) post-merging section

acceptance range from 140 MeV/c to 220 MeV/c. Three types of 352 MHz RF with different lengths are employed from the stage 1 to stage 4. The selection of two additional longer cavity lengths is motivated by the objective of reducing the peak RF gradient and accommodating the RF cavities within the cooling cell. The cooling cell gets shorter in later stages to achieve tighter focusing and reduce the transverse beta function. However, tighter focusing means the cell has a poorer longitudinal momentum acceptance. Therefore, it is important to gradually decrease the cell length and transverse beta function in each stage to match the momentum spread of the muon beam with the momentum acceptance. The final cooling system requires the input transverse emittance to be less than 0.3 mm which is achieved at the end of the stage 8. However, we find it is still possible to further reduce the emittance

by adding two more stages with moderate particle loss. The evolution of emittance and merit factor are shown in Fig. (5b) and Fig. (6b), respectively. The particles distribution in the phase space of the post-merging section is displayed in Fig. (7d), (7e) and (7f). We also calculate the theoretical emittance for the end of each stage in the post-merging section from the Eqs.(11) and (12) and the results are shown in Table IV. The initial emittance in the Eq.(11) is equal to the simulated emittance at the end of each stage. Compared with the simulation results shown in Table III, the largest discrepancy between theory and simulation is 24.6%. This discrepancy between the simulation and theoretical predictions is expected, given that the theory is entirely linear and treats transverse and longitudinal beam motion separately. In most cases, the theory yields higher output emittance at the end of each stage. This discrep-
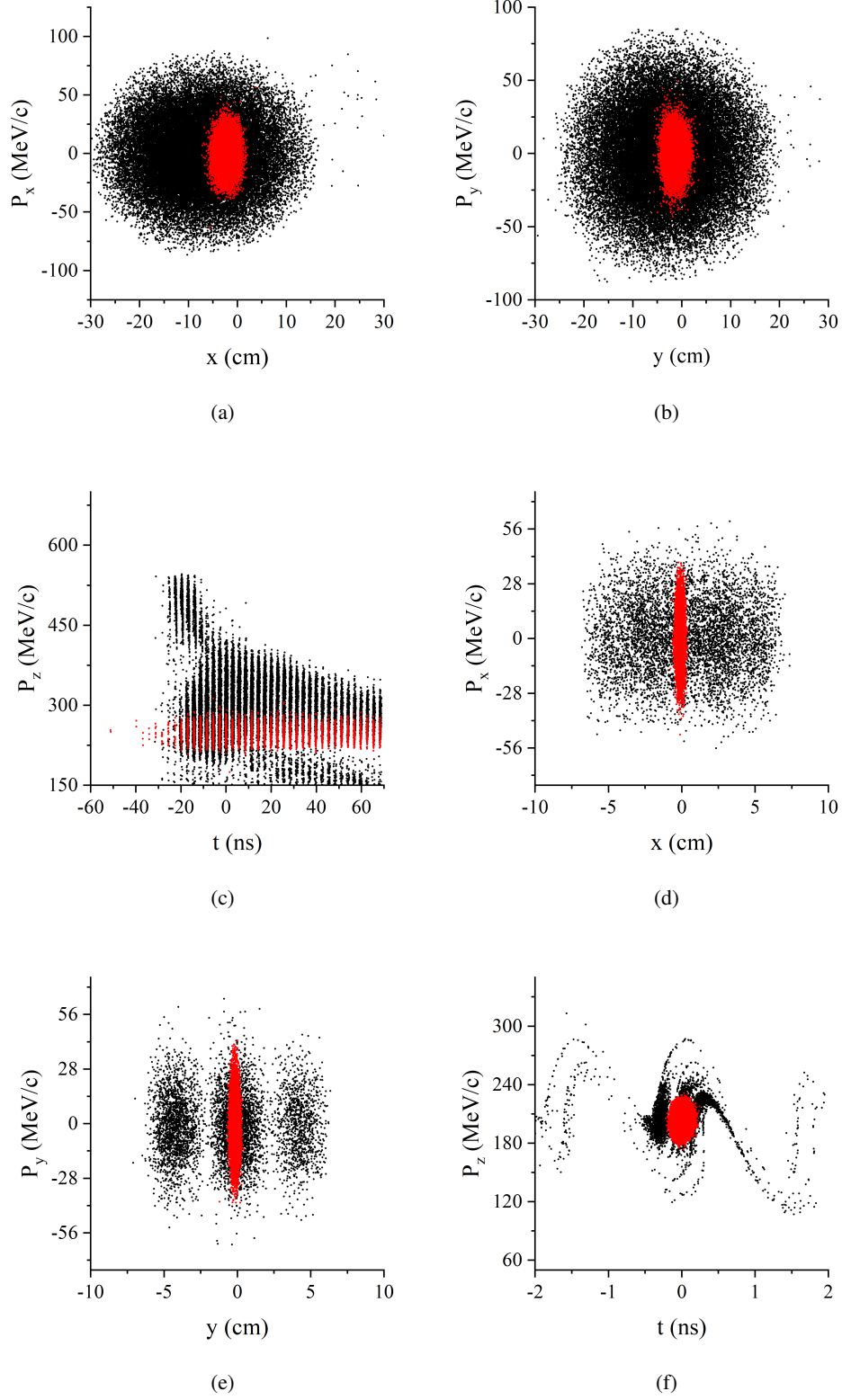
FIG. 7: Particles distribution in the phase space: (a), (b), (c), pre-merging section; (d), (e), (f), post-merging section (black and red dots denote the distribution at the start and the end of the cooling section respectively)

TABLE III: Simulation results on the normalized emittance and transmission at the end of each stage after merging

	$\varepsilon_{T,sim}$ (mm)	$\varepsilon_{L,sim}$ (mm)	$\varepsilon_{6D,sim}$ (mm^3)	Transmission
Start	5.129	9.991	262.5	
B-Stage 1	2.901	8.945	76.07	85.2%
B-Stage 2	2.096	5.964	26.68	89.2%
B-Stage 3	1.271	4.055	6.795	87.6%
B-Stage 4	0.9314	3.200	2.793	91.3%
B-Stage 5	0.7130	2.508	1.323	89.4%
B-Stage 6	0.4881	2.306	0.5571	87.9%
B-Stage 7	0.3712	2.114	0.2953	91.2%
B-Stage 8	0.2595	1.920	0.1304	88.2%
B-Stage 9	0.1892	1.728	0.06149	85.3%
B-Stage 10	0.1387	1.564	0.03006	86.9%

TABLE IV: Theory results on the normalized emittance at the end of each stage in the post-merging section and error between the theory and simulation

	$\varepsilon_{T,theo}$ (mm)	Err$_T$	$\varepsilon_{L,theo}$ (mm)	Err$_L$
B-Stage 1	3.119	7.0%	8.614	3.8%
B-Stage 2	2.616	19.9%	5.338	11.7%
B-Stage 3	1.665	23.7%	3.559	13.9%
B-Stage 4	1.113	16.3%	2.967	7.9%
B-Stage 5	0.8083	11.8%	2.568	2.3%
B-Stage 6	0.5099	4.3%	2.540	9.2%
B-Stage 7	0.4158	10.7%	2.130	0.75%
B-Stage 8	0.3442	24.6%	1.703	12.7%
B-Stage 9	0.2477	23.6%	1.659	4.0%
B-Stage 10	0.1832	24.3%	1.647	5.0%

ancy arises primarily because the theoretical model does not account for particle loss.

In summary, the 10-stage post-merging cooling section is able to reduce the normalized transverse and longitudinal emittance of the muon beam from 5.129 mm and 9.991 mm to 0.1387 mm and 1.564 mm, respectively. The channel length is 487.47 m with the transmission of 28.5% including the muon decays. The output transverse emittance of this updated design is half that of the previous design [11]. A lower initial transverse emittance is always beneficial for the final cooling. Previous simulation studies on final cooling have successfully reduced the normalized transverse emittance of the muon beam to 55 μm [28]. The current studies initiated by the International Muon Collider Collaboration (IMCC) aspire to surpass this achievement, aiming for a value as low as 25 μm [2]. We anticipate that the output muon beam of this updated post-merging rectilinear cooling channel design will significantly facilitate the final cooling system to achieve the goal of a normalized transverse emittance of 25 μm.

V. TRACKING SIMULATION USING π-MODE RF AND ERROR ANALYSIS

The International Muon Collider Collaboration proposes a 6D muon cooling demonstrator with the aim of demonstrating the 6D emittance reduction using the initial muon beam with modest emittance. The π-mode RF offers numerous advantages, such as its compact waveguide structure and the requirement for only one RF coupler and cryo-module feedthrough to supply all the RF cells. These characteristics make it the potentially ideal candidate for the baseline design of the cooling demonstrator [29]. However, due to the fact that the length of the π-mode RF cavity is half of its wavelength, it is considerably longer than the cavity used in Section IV. Consequently, this results in a lower transit time factor, as defined in Eq. (27).

$$T = \frac{\sin \omega_{rf} L/2\beta c}{\omega_{rf} L/2\beta c} \quad (27)$$

where ω_{rf} is the angular frequency of the RF, L is the length of the RF and βc is the speed of the reference particle. For the same RF length and phase, a lower transit time factor means a higher RF gradient for restoring the same energy loss in the absorber, as seen from Eq. (28).

$$\Delta E_{rf} = N_{cav} T V_{rf} L \sin \varphi_s \quad (28)$$

where ΔE_{rf} is the energy gain from the RF, N_{cav} is the number of RF cavities, T is the transit time factor, L is the length of each RF cavity and φ_s is the RF phase.

As the initial emittance of stage 5 in the post-merging cooling section is similar to that in [12], we choose the cooling cell in stage 5 as a baseline to check the impact of the π-mode RF on cooling performance. Since the length of the π-mode RF cavity is 18.8 cm, nearly double that of the standard cavity discussed in Section IV, we have increased the length of the cooling cell from 80 cm to 90 cm. The lattice parameters and tracking results of the emittance and transmission for the two cases of π-mode and normal mode RF are summarized in Table V and Table VI, respectively. In order to only investigate if the π-mode RF influences the cooling performance, we maintain identical magnetic field and wedge absorber settings in both cases, with the only differences being in the RF length, gradient, and phase. The tracking results in Table VI indicate that there is no obvious difference in cooling performance between the normal and π-mode cases. From Table V, it is evident the π-mode RF has higher peak gradient and phase compared with the normal mode, which is due to a lower transit time factor.

To investigate the robustness of the cooling lattice using the π-mode RF, error analysis studies are conducted. Two sources of errors are considered: those originating from the solenoid coils and the RF cavities. For the solenoid coils, errors are classified into three types: current, position, and rotation. For the RF cavities, errors are classified into four types: gradient, phase, position and rotation. The steps of a simulation for a

specific error are as follows: (a) Generate random numbers (errors) from a Gaussian distribution; (b) Apply these errors to the solenoid coils or RF cavities in the simulation. (c) Repeat step (a) and (b) for 50 iterations. (d) Average the output

emittance and transmission from these 50 simulation results.

VI. CONCLUSIONS

[1] J. D. Jackson, *Classical Electrodynamics, 3rd ed* (1999).

[2] C. Accettura, D. Adams, and R. e. a. Agarwal, Towards a muon collider, Eur. Phys. J. C **83**, 10.1140/epjc/s10052-023-11889-x (2023).

[3] M. Bogomilov, R. Tsenov, and G. V.-K. et al., Demonstration of cooling by the muon ionization cooling experiment, Nature **578**, 10.1038/s41586-020-1958-9 (2020).

[4] M. Bogomilov, R. Tsenov, and G. V.-K. et al., emittance reduction in muon beams by ionization cooling (2023), arXiv:2310.05669 [physics.acc-ph].

[5] D. Neuffer, Introduction to muon cooling, Nucl. Instrum. Methods Phys. Res., Sect. A **532**, 26 (2004).

[6] R. Palmer, V. Balbekov, J. S. Berg, S. Bracker, L. Cremaldi, R. C. Fernow, J. C. Gallardo, R. Godang, G. Hanson, A. Klier, and D. Summers, Ionization cooling ring for muons, Phys. Rev. ST Accel. Beams **8**, 061003 (2005).

[7] P. SNOPOK, G. HANSON, and A. KLIER, Recent progress on the 6d cooling simulations in the guggenheim channel, International Journal of Modern Physics A **24**, 987 (2009).

[8] Y. Derbenev and R. P. Johnson, Six-dimensional muon beam cooling using a homogeneous absorber: Concepts, beam dynamics, cooling decrements, and equilibrium emittances in a helical dipole channel, Phys. Rev. ST Accel. Beams **8**, 041002 (2005).

[9] V. Balbekov, Muon accelerator program document no. 4365, (2013).

[10] D. Stratakis, R. C. Fernow, J. S. Berg, and R. B. Palmer, Tapered channel for six-dimensional muon cooling towards micronscale emittances, Phys. Rev. ST Accel. Beams **16**, 091001 (2013).

[11] D. Stratakis and R. B. Palmer, Rectilinear six-dimensional ionization cooling channel for a muon collider: A theoretical and numerical study, Phys. Rev. ST Accel. Beams **18**, 031003 (2015).

[12] C. Rogers, A demonstrator for muon ionisation cooling, Physical Sciences Forum **8** (2023).

[13] A. Grudiev, Considerations on isolated rf cells or multicells, in *MuCol WP8 Cooling Cell Workshop)* (2024).

[14] J. Yang, J. Xia, and G. X. et al., High intensity heavy ion accelerator facility (hiaf) in china, Nucl. Instrum. Methods Phys. Res., Sect. B **317**, 263 (2013).

[15] C. Caso *et al.* (Particle Data Group), Review of particle physics. Particle Data Group, Eur. Phys. J. C **3**, 1 (1998).

[16] D. Neuffer, Comments on ionization cooling channels, Journal of Instrumentation **12** (09), T09004.

[17] U. Fano, Penetration of protons, alpha particles, and mesons, Annual Review of Nuclear and Particle Science **13**, 1 (1963).

[18] G. Franchetti, Linear beam optics in solenoidal channels, Phys. Rev. ST Accel. Beams **4**, 074001 (2001).

[19] C.-x. Wang and K.-J. Kim, Recursive solution for beam dynamics of periodic focusing channels, Phys. Rev. E **63**, 056502 (2001).

[20] P. Virtanen, R. Gommers, and T. E. e. a. Oliphant, SciPy 1.0: Fundamental Algorithms for Scientific Computing in Python, Nature Methods **17**, 261 (2020).

[21] T. J. Roberts and D. M. Kaplan, G4beamline simulation program for matter-dominated beamlines, in *2007 IEEE Particle Accelerator Conference (PAC)* (2007) pp. 3468–3470.

[22] R. C. Fernow, *Physics analysis performed by ECALC9*, Tech. Rep. (2003).

[23] D. Bowring, A. Bross, P. Lane, M. Leonova, A. Moretti, D. Neuffer, R. Pasquinelli, D. Peterson, M. Popovic, D. Stratakis, K. Yonehara, A. Kochemirovskiy, Y. Torun, C. Adolphsen, L. Ge, A. Haase, Z. Li, D. Martin, M. Chung, D. Li, T. Luo, B. Freemire, A. Liu, and M. Palmer, Operation of normal-conducting rf cavities in multi-tesla magnetic fields for muon ionization cooling: A feasibility demonstration, Phys. Rev. Accel. Beams **23**, 072001 (2020).

[24] B. D. Muratori, J. K. Jones, and A. Wolski, Analytical expressions for fringe fields in multipole magnets, Phys. Rev. ST Accel. Beams **18**, 064001 (2015).

[25] H. Enge, *Focusing of Charged Particles* (Academic Press, 1967).

[26] C. T. Rogers, D. Stratakis, G. Prior, S. Gilardoni, D. Neuffer, P. Snopok, A. Alekou, and J. Pasternak, Muon front end for the neutrino factory, Phys. Rev. ST Accel. Beams **16**, 040104 (2013).

[27] Y. Bao, G. Hanson, R. B. Palmer, and D. Stratakis, Conceptual design and modeling of a six-dimensional bunch merging scheme for a muon collider, Phys. Rev. Accel. Beams **19**, 031001 (2016).

[28] H. Kamal Sayed, R. B. Palmer, and D. Neuffer, High field – low energy muon ionization cooling channel, Phys. Rev. ST Accel. Beams **18**, 091001 (2015).

[29] R. Losito, L. Rossi, C. Barbagallo, J. S. Berg, L. Bottura, G. Burt, M. Castoldi, S. Fabbri, G. Ferrand, and J. A. Ferreira Somoza, Presentation of cooling cell conceptual design.

TABLE V: Main parameters of the cooling cell for π-mode and normal mode RF

	Cell length (m)	Stage length (m)	Max. on-axis B_z (T)	Integrated B_y (T·m)	Transverse beta (cm)	Dispersion (mm)	On-axis wedge length (cm)	Wedge apex angle (deg)	RF frequency (MHz)	Number of RFs	RF length (cm)	Transit time factor	Max. RF gradient (MV/m)	RF phase (deg)
π-mode	0.9	42.3	8.1	0.105	10	-17.5	12	120	704	3	18.8	0.63	26.3	23.8
normal mode	0.9	42.3	8.1	0.105	10	-17.5	12	120	704	5	9.5	0.90	22.3	23.0

TABLE VI: Simulation results on the normalized emittance
and transmission of the normal and π-mode lattice

	$\varepsilon_{T,sim}$ (mm)	$\varepsilon_{L,sim}$ (mm)	$\varepsilon_{6D,sim}$ (mm^3)	Transmission
Start	0.9101	3.261	2.795	
π-mode	0.7142	2.539	1.326	90.4%
Normal mode	0.7088	2.516	1.299	90.1%